A micro fuel cell for abiotical catalysis of glucose

Do, Uyen Phuong[1]; Seland, Frode[2]; Johannessen, Erik Andrew[1]

[1]Department of Microsystems, Faculty of Technology, Maritime and Natural Sciences, University of South-Eastern Norway, Raveien 215, 3184 Borre, Norway
[2]Department of Materials Science and Engineering, Faculty of Natural Sciences and Technology, Norwegian University of Science and Technology, NTNU 7491 Trondheim, Norway

Do, U. P., Seland, F. & Johannessen, E. A. (2020). A micro fuel cell for abiotical catalysis of glucose. Journal of Power Sources, 478, 229032. https://doi.org/10.1016/j.jpowsour.2020.229032

A micro fuel cell for abiotical catalysis of glucose

Uyen Phuong Do[1]
Frode Seland[2]
Erik A. Johannessen[1]

Received: date / Accepted: date

[1]Department of Microsystems, Faculty of Technology, Maritime and Natural Sciences, University of South-Eastern Norway, Raveien 215, 3184 Borre, Norway

[2]Department of Materials Science and Engineering, Faculty of Natural Sciences and Technology, Norwegian University of Science and Technology, NTNU 7491 Trondheim, Norway

Corresponding author, E. A. Johannessen: eaj@usn.no

Keywords: glucose fuel cell, stacked electrodes, abiotic catalysis, Pd cathode, Pt-Ni anode, simplified FEM model

Abstract:

A miniaturised abiotical fuel cell designed for operation inside a physiologically relevant mixed fuel environment of dissolved di-oxygen (DO) and glucose, have been realised by embedding the glucose sensitive anode below a porous oxygen scavenging cathode. Experimental results showed the cell capable of maintaining a power density of 2.33 ± 0.11 μW cm^{-2} at a current density of 7.7 μA cm^{-2} and a cell potential of 0.30 ± 0.01 V. This is comparable to a simulated result of 7.9 μA cm^{-2} in which the DO concentration from the bulk solution of 60 μM (2 ppm) were predicted to have fallen to 35 μM (1.18 ppm) before entering the cell and reacting with the anode. In contrast, the flux of glucose supplied to the anode was found to maintain a concentration of 3.7 mM inside the cell (from a bulk concentration of 5 mM). The generated power was approximately 80% of the recorded peak power density of 2.83 ± 0.24 μW, that was obtained from separating the fuels prior to use. This suggests that the proposed design were able to limit the amount of DO entering the cell prior to catalysis, and thereby minimize any reduction in the overall current density.

1 Introduction

Smart sensor systems that is linked to the internet and senses the physical world around us came of age from the merger between microfabricated sensors with low-power computing systems. Their small physical footprint rendered these as interesting candidates for a new generation of medical devices that may track an ailment inside the body without any major surgical intervention. Popular device applications range from wireless pacemakers [1], to defibrillators [2], neurostimulators [3], insulin pump [4], glucose sensors [5], ID tags [6], cochlear [7] and retinal implants [8] and potential brain machine interfaces [9].

A prerequisite for reliable use is a viable power supply that will not limit their operational lifetime once implanted inside the body. The current norm uses endogenous energy in the form of batteries as envisaged in cardiac pacemakers and deep brain stimulators [10], [11], but their storage capacity scales with size which will limit the constraints of a miniaturized implant. Attempts using inductive energy transfer (as demonstrated in cochlear implants) yields an external power supply unit [12] but these only work over short distances and scales with the antennae dimension. Consequently, energy harvesting from the local environment may represent a viable alternative for power conversion from a source that may not be depleted with time. These range from the use of thermal gradients [13], to mechanical vibration [14], and exogenous chemicals [15] – the latter especially in the context of a physiological environment, where biological fuels such as glucose and dissolved di-oxygen (DO) exits in relative abundance. The use of exogenous chemicals may be realised through a fuel cell system whose nature depend on the type of catalyst that governs the oxidation process. Enzymatic fuel cells use isolated enzymes such as glucose oxidase or hexokinase that are immobilized directly on the electrode surfaces [16],[17], whereas microbial fuel cells utilise whole living micro-organisms such as bacteria and yeast that converts glucose completely to its end products CO_2 and water [18],[19],[20]. Abiotic fuel cells on the other hand is based on non-biological materials such as activated carbon or noble metals and their alloys [21],[22],[23],[24] which bypasses the fragile nature of the biocomponents with the drawback of lower power densities and conversion efficiency [25]. Catalytic materials for use in the glucose oxidation process have been reported since the first attempts of abiotic glucose oxidation was published back in 1964 [26].

The power generating capabilities range from mW cm^{-2} (enzymatic) to uW cm^{-2} (microbial and abiotical), with a voltage output limited to 1.3 volts (theoretical) at standard conditions [21]. The loss due to ohmic and reaction overpotentials renders these significantly lower in practical use with the peak power generated at a cell potential in the tens of a voltage range [16],[17], [18], [19], [20], [21], [22], [23], [24]. Since most microelectronic devices require more than one volt to function, the output potential from these cells must be ramped up prior to use. The most conventional way would be to stack the fuel cells in series [27], or ramping up the voltage using a DC-DC converter (charge pump) [28]. The charge generated can also be stored in a capacitor for subsequent use given that most system would not need to be continuously powered up [29]. Although an increase in the effective surface area of the fuel cell may meet the current consumption of the electronic device, circuit modules targeting consumption in the uA regime is now being developed [30],[31],[32].

The catalyst used in fuel cell electrodes has traditionally been based on platinum (Pt) and its alloys including non-noble metals such as Raney-Pt [21],[33],[34]. When implemented in a cathode for oxygen reduction, these materials are also sensitive for glucose oxidation which renders them less suitable for use in environments where both glucose and DO are mixed together (such as the human body). Alternative materials such as activated carbon exhibits

lower catalytic activity towards oxygen reduction [35], whereas silver, gold or ferric phthalocyanine combines a higher catalytic activity towards glucose oxidation with a reduced catalytic activity towards oxygen reduction compared to Pt [21]. In contrast, palladium (Pd), which shares some of the qualities of Pt, as well as its application in fuel cells, hydrogen sensors and catalytic converters [21],[36],[37], has been characterized as a catalyst in extreme alkaline and acidic media as well as neutral solutions with pH of 7.4 [21],[25],[36],[37]. It is in particular the ability to maintain a high catalytic activity of oxygen reduction in the presence of glucose that has proven interesting [25]. It is also readily implemented as thin films in micro fabrication processes through sputtering, evaporation, chemical synthesis or electrodeposition [36],[37],[38].

In contrast, Pt is a good candidate particularly in acidic electrolytes or mediums [39] considering the glucose oxidation process only. Other abiotic catalysts such as gold and palladium offers best performance in neutral and alkaline media, respectively [39],[40],[41]. One main drawback of implementing these materials in an anode is the loss of catalytic activity with time due to a “poisoning” effect [39], where the active surface sites becomes blocked from the formation of reaction intermediates such as carbon monoxide that bonds strongly to the surface [42]. Hence, the combination of non-noble metals such as Zinc (Zn), Lead (Pb), Nickel (Ni) or Aluminium (Al) with Pt into Raney-Pt alloys may offer more promising results. These exhibit a reduced “poisoning” effect and are able to maintain a good catalytic activity towards glucose oxidation [11, 33, 43, 44], though all of these do also catalyse oxygen reduction.

Consequently, the use of a fuel cell in an environment where both glucose and DO are present requires some means of separation before they are consumed. This was first addressed by Drake, Rao and von Sturm back in the 1970’s when glucose fuel cells were considered a potential alternative powering the artificial pacemaker [45],[46],[47]. It was not until the advent of low power miniaturised sensor systems in the early 2000s that the glucose fuel cell was given a renaissance with work presented by Rapoport, Kerzenmacher, Oncescu, and Stetten [11],[21],[44],[48]. Since the transport of reactants occurs by diffusion, the proposed solution was to stack the fuel cell assembly with a porous oxygen selective cathode positioned on top of a (non-selective) anode below. As the reactants start to diffuse through the pores, some of the oxygen should be removed by the cathode before coming into contact with the anode.

This paper presents a model that evaluates the ability to remove oxygen from the mixture with glucose and to predict how the cathode and anode will perform in such a setting. The geometric parameter of the pore was tuned to the results from the cathode fabrication process [25], and the fuel cell was characterized under a simulated physiological condition with glucose and oxygen mixed together, as well as being treated as separated reagents for comparison. This fuel cell system makes solemn use of evaporated thin film catalysts that is compatible with modern microfabrication methodologies. This is in contrast to prior work where the electrode system in part consists of thick film catalyst based on active carbon in particle or mesh form [48],[44],[49] as inks [22], nanotubes [11], nanofibers [23] or as electroplated catalyst coated on metal foils [50]. The separation of reactants is realized through the use of a nanoporous cathode made from anodic aluminum oxide (AAO).

2 Materials and Methods

2.1 Device fabrication

The fabrication of the cathode and the anode have previously been reported in [25],[51]. The cathodes were produced by e-beam evaporation of a 200 nm thick Pd film acting as the oxygen selective catalyst on top of a nanoporous AAO membrane (Anodisc 6808-7023, Fisher Scientific, UK) with a diameter of 13 mm and with pores ranging from 100 to 200 nm. The anodes were made by e-beam evaporation of 20 nm Titanium (Ti), 100 nm Pt and 300 nm Ni on a single side polished, <100>, 4" Si wafers (p-type, 525 ± 25 µm thickness, Si-Mat, Germany). The electrodes where diced into 5x5 mm samples by a dicing saw (DAD - 2H/6T, Disco Corp., Japan) and annealed in a 2" barrel furnace (MSL, MTI Corp., USA) at a temperature of 800°C for 2 hours in an inert atmosphere of N_2 at a flow rate of 2 L min^{-1}. Unalloyed Ni was etched away in a solution of (1:1 volume) of 1 M sulfuric acid (H_2SO_4) and 0.39 m nitric acid (HNO_3) at 80°C for 2 hours. Electrical connection of all electrodes was made by using silver epoxy (EPO-TEK EE129-4, Epoxy Technology, Inc., US) to bond a copper wire to the metal surface prior to encapsulation by silicone rubber (3140 RTV Coating, Dow Corning, US). Finally, cyclic voltammetry in 1 M H_2SO_4 solution at 80 °C were used to electrochemically etch any remaining Ni and nickel oxide on the anode surface by scanning a potential from -0.30 to 0.40 V at a scan rate of 10 mV s^{-1} over 10 cycles (Versastat 3, Princeton Instruments, US).

A standard Ag|AgCl reference electrode in 4 M saturated KCl (Thermo Scientific, US) was used as the reference electrode whereas a coiled up Pt wire (P/3640/89, Fisher Scientific Limited, UK) was used as the counter electrode. Electrical connection of all electrodes was made by using silver epoxy (EPO-TEK EE129-4, Epoxy Technology, Inc., US) to bond a copper wire to the metal surface prior to encapsulation by silicone rubber (3140 RTV Coating, Dow Corning, US). The fuel cell housing was machined from solid polyetheretherketone (PEEK, FossTech as, Norway) whereas the membrane support layer was made from stainless steel (Easycad Oy, Finland). The porous frit U-tube (product code: 44454-00) was supplied by PHYWE Systeme GmbH, Germany.

2.2 Proposed fuel cell design

The electrodes should be arranged so that the fluid with the mixed reactants (glucose and oxygen) can be utilised by separating the oxygen away from the glucose. This can be achieved by placing the oxygen "consuming" cathode first in the diffusion pathway of the reagents so that most of the oxygen has been removed before the reagents reaches the anode (Figure 1). In this proposed design, the porous cathode is positioned with the catalytic Pd layer facing up. Both oxygen and glucose will diffuse down towards the cathode surface, where a reduction of oxygen will take place once in contact with the Pd catalyst. With "most" of the oxygen removed, glucose will diffuse further into the cell, and become oxidised to gluconic acid by the Pt-Ni catalyst on the anode surface. The gluconic acid will in turn diffuse out of the cell. The two electrons that are released for every glucose molecule oxidised will be channelled (through an electric circuit where work can be performed) back to the cathode to facilitate the reduction of the O_2 molecule. The protons released at the anode interface will be conducted back to the cathode through the electrolyte separator and transported out from the pores by diffusion. A solid proton conducting electrolyte such as Nafion or polyethersulfone can be replaced with a standard buffer if the

distance between the two electrodes is kept to a minimum so that the diffusion layers overlap. In this manner proton "conduction" can be assumed to occur by diffusion alone.

2.3 Model of glucose and oxygen diffusion

The pore size of the cathode is a trade-off between the cavity area providing flow by diffusion of reagents and the surface area required to maintain a catalytic activity that is high enough to remove DO from the solution. The deposition of the Pd film offered an additional method to "shrink" the pore size on the top (entrance) of the porous cathode as a function of the film thickness. The sample rotation was made at an angle during the catalyst deposition in order to improve the coverage around the pore rim and on the pore wall, which would increase the effective area of the catalyst [25].

A model was made and simulated in COMSOL Multiphysics (COMSOL Inc., US) in order to investigate these effects (Figure 2). The module "Transport of Diluted Species" was used and the cathode was modelled as a single pore element consisting of a cylinder with diameter (d_{Bot}) located within a given cross section (w = 1 µm) of the cathode (equivalent to $1x10^8$ pores cm^{-2}). The reduced diameter near the top of the pore entrance was modelled as a funnel with diameter (d_{Top}) and catalyst film thickness (t_m). The thickness of the membrane support structure (the AAO substrate material) representing the length of the pore channels was set to t_b = 60µm. Although an increase in the catalyst film thickness (t_m) could narrow the pore size at the top surface (d_{Top}) in the real experiment, there are still a large variety of pore sizes due to the imperfection in the AAO membrane production. Hence, both t_m and d_{Top} were considered as two independent factors in this model. The thickness of the proton conducting electrolyte (Nafion® PFSA NR211, DuPont, US) located between the cathode and the anode (t_{Naf}) was set to 28 µm [52]. The thickness (t_d) of 100 µm corresponded to the diffusion layer between the cathode surface and the surrounding bulk solution [50],[53] which considered all flow in the vicinity of the cell being laminar in origin [54]. The parameters used in this model were taken from the experiment presented in [25].The pore size of the membranes (d_{bot}) was set to an average diameter of 100 and 200 nm according to the specifications given of the 60 µm thick commercial AAO membranes used (Anodisc 6809-7013 and 6809-7023, Fisher Scientific, UK). The range of the catalyst film thickness (t_m) ranged from 100 to 200 nm [25]. The diameter of the pores at the top rim (d_{Top}) were selected in the range from 20 to 90 nm (d_{Bot} = 100 nm) and 50 to 190 nm (d_{Bot} = 200 nm), respectively.

The bulk concentration was kept at 5 mM for glucose [21], and 60 µM (2 ppm) for DO [55]. This corresponds to the physiological levels found in human subcutaneous tissue. As an initial boundary condition, it was assumed that oxygen was consumed completely at the catalyst surface of the cathode (zero molar concentration - value set by the program according to the diffusion gradient). A second condition was also explored in which the cathode failed to remove all oxygen resulting in DO diffusing through and becoming catalysed at the anode (values set by the simulated results). Although some of the glucose would be oxidised at the cathode surface, the assumption was made that this electrocatalysis would not bear a significant impact on the overall external glucose concentration entering the cell.

The calculation of the maximum (simulated) current density (j_{FC}) was based on the reactant flux of oxygen at the cathode and glucose at the anode by the following expressions [50]:

Cathodic:

$$j_{FC} = \frac{F_C n_C F}{A_C} \quad \textbf{Equation 1}$$

Anodic:

$$j_{FC} = \frac{F_A n_A F}{A_A} \quad \textbf{Equation 2}$$

where F_C and F_A are the reactant flux at the cathode and anode respectively (mol s^{-1}), n_C and n_A are the number of transferred electrons per oxygen and glucose molecule consumed, F is Faradays constant (= 96485 C mol^{-1}), and A_C and A_A are the geometric area of cathode and anode respectively (cm^2). This is based on the individual area of the pore model (10^{-8} cm^2 for the anode, and (10^{-8} – π * $d_{Top}^2/4$) cm^2 for the cathode). In this case, n_C = 4 and n_A = 2 according to the following reactions:

Cathodic: $O_2 + 2H_2O + 4e^- \rightarrow 4OH^-$

Anodic: $C_6H_{12}O_6 + 2OH^- \rightarrow C_6H_{12}O_7 + H_2O + 2e^-$

The diffusion of solutes in narrow pores can be expressed by the Renkin equation [56],[57]:

$$\frac{D_m}{D_0} = \left(1 - \frac{R_S}{R_P}\right)^2 * \left[1 - 2.104\left(\frac{R_S}{R_P}\right) + 2.09\left(\frac{R_S}{R_P}\right)^3 - 0.95\left(\frac{R_S}{R_P}\right)^5\right] \quad \textbf{Equation 3}$$

where D_m and D_0 are the solute diffusivity in the membrane and in the free solution, respectively; R_S and R_P are the solute radius and the pore radius respectively. In this case, the diffusivity of glucose is set at $D_{0\text{-}Gluc}$ = 6.73 x 10^{-6} (cm^2 s^{-1}) whereas the radius is $R_{S\text{-}Gluc}$ = 4.44 (Å) [57]. The diffusivity of oxygen is $D_{0\text{-}Oxy}$ = 1.2 x 10^{-5} (cm^2 s^{-1}) [58] and with a radius of $R_{S\text{-}Oxy}$ = 1.73 (Å) [59].The diffusivity of oxygen and glucose through the Nafion membrane is 1.04 x 10^{-6} (cm^2 s^{-1}) and 3.4 x 10^{-8} (cm^2 s^{-1}) respectively [52],[59]. As shown in the relationship between the pore diameter and the diffusion coefficient of glucose as well as oxygen inside the pore in Figure 2.b, the effect of pore diameter on the diffusion coefficients of both glucose and oxygen will be significant if the pore diameter is less than 40 nm. The transport by diffusion follows the concentration gradient along the z-axis of the pore and could be simplified to 1D according to the Fick's law of diffusion:

$$F_i = -D_i * \nabla C_i = -D_i * \frac{\Delta C_i}{\Delta z_i} \quad \textbf{Equation 4}$$

where the subscript i stands for either oxygen or glucose, the values of the diffusivity D_i (cm^2 s^{-1}), the concentration gradient ΔC_i (M) and the distance Δz_i (cm) over which the concentration gradient extends.

2.4 Fuel cell test and assembly

The electrochemical performance of the glucose fuel cell with the given catalysts were tested in a solution of 10 mM PBS (P3813, Sigma-Aldrich, US) at pH 7.4. All the experiments were taken at room temperature. Glucose was added (G7525, Sigma-Aldrich, US) to a concentration of 5 mM to simulate the physiological levels in subcutaneous tissue [21]. The corresponding amounts of air and nitrogen (N_2) were mixed and pumped into the test vessel in order to obtain the required DO concentration which was continuously monitored by DO meters (C3040, Consort, Belgium). A DO concentration of 60 µM $\cong$ 2 ppm $\cong$ 7% was selected from the value found in the subcutaneous tissue, a proposed location of the fuel cell and medical implant [55]. A potentiostat (Versastat 3, Princeton Instruments, US) was used to obtain the polarization curves of the glucose fuel cell. Stable potential values were achieved by applying a current step of 1.1 µA cm^{-2} for a period of 2 h from an initial open circuit potential (OCP).

Two experimental setups were explored (Figure 3): (i) a standard U-tube assembly and (ii) a stacked fuel cell package according to the proposed design (section 2.2). The two compartments of the U-tube (Figure 3a) was separated by a porous glass frit that allowed ionic communication between the anodic and cathodic compartment. It also acted as a barrier preventing the mixture of the two reactants (oxygen and glucose) within the timeframe of the experiment. The U-tube vessel was used as a proof-of-concept to simulate the “best” case scenario (denoted U1), in which DO and glucose was added as separate reagents. It also considered the “worst” case scenario (denoted U2), in which DO and glucose was mixed at both electrodes. In the “best” case scenario (U1), PBS with 5 mM glucose was added in the right hand compartment containing the anode (and deoxygenated with N_2), whereas PBS without glucose was added to the left hand compartment containing the cathode using N_2 gas to reduce (and maintain) the DO concentration to 60 µM. In the “worst” case scenario (U2), the PBS solution was mixed with 5mM glucose and 60 µM DO in both compartments. The cathode and anode electrodes were attached on a glass slide by silicone rubber prior to being mounted in their separate compartments of the U-tube (Figure 3a). The U-tube was not plugged to allow excess N_2 gas to be expelled.

The stacked fuel cell assembly was designed in house, and consisted of a 13 mm circular porous Pd cathode positioned with the catalyst film facing up on top of a 5x5 mm Pt-Ni anode with a 5x5 mm large Nafion film stacked in between. This stacked “fuel cell core” was inserted into a carrier made from polyetheretherketone or PEEK (Figure 3 b,c) and immersed in PBS containing both 5 mM glucose and 60 µM DO to simulate a real *in vivo* test condition (denoted U3). The electrical separation and ionic conduction between two electrodes were realized by the PBS filled channels of the porous AAO membrane and the Nafion film. An o-ring was used to separate the cathode from the protective metal frame at the top surface of the carrier. Silicone rubber sealed of the gap at the wall between the anode, the Nafion film and the cathode to ensure that the test solution could only access the anode throught the pores of the cathode.

3 Results and discussion

3.1 Transport by diffusion I - Simulation

The total oxygen flux (F_{Tot}) associated with a single pore element (Figure 4), consists of the DO flux at the top surface of the cathode (F_{Top}) as well as the DO flux penetrating the inclined walls of the pores covered with catalyst (F_{Incl}). These fluxes are presented as a function of the pore geometry, including the original pore size d_{Bot}, the reduced pore size at the top surface d_{Top} and the catalyst thickness t_m.

The concentration gradient were considered to occur in the z-direction from the bulk solution concentration (60 µM) and down to the top surface of the cathode over a diffusion layer thickness (t_d) of approximately 100 µm. The concentration of DO at the cathode surface will be a function of the catalytic activity of the anode feeding the cathode with electrons. Any residual DO at the cathode surface will penetrate the pore, and have its maximum concentration at the centre axis of the inclined portion due to radial diffusion toward the pore wall and the residing catalyst. The ratios between the oxygen gradient in the pore centre and distance to the pore wall will be smaller than the equivalent values between the bulk solution and the gradient at the top surface. Since the catalyst area of the top surface is larger than the area of the inclined portion of the pore, any change in the total oxygen flux will mainly depend on flux rate at the top surface.

The initial consideration that all the DO have been reduced at the electrode surface (zero mM) will create a maximum concentration gradient from the bulk solution, and a corresponding ideal maximum flux rate. The oxygen flux at the inclined pore wall (F_{Incl}) is found to increase with the pore size d_{Top} due to an increased flux of DO into the pore combined with a larger surface area of the pore rim (Figure 4a). For d_{Top} in the range of 50 to 90 nm, the F_{Incl} was larger for the pores with a base diameter (d_{Bot}) of 100 nm compared to those with a base diameter of 200 nm. This difference of 1.18 ± 0.03 times (measured at d_{Top} = 90 nm) is most likely a result of an average shorter radial diffusion distance from the pore centre to the inclined pore wall. However as the pore size extends beyond 90 nm, data was only obtainable from samples with the larger base diameter.

The DO flux at the top surface (F_{Top}) reduces with increased pore diameter, but has an indecipherable change with t_m. This suggests that the contribution from the inclined pore section of the catalyst layer is marginal. If we consider the main part of the oxygen diffusion happening vertically along the z-axis, the theoretical oxygen flux at the top surface of the cathode, estimated by Eq 4**,** would be the equivalent of $7.8 * 10^{-19}$ mol s^{-1} which is in good agreement with the F_{Top} data achieved by the simulation for d_{Top} = 20 nm.

The total DO flux (F_{Tot}), including the flux at the top surface (F_{Top}) and at the inclined pore wall (F_{Incl}), is shown as a function of the pore geometrics parameters in Figure 4b. The response scales with d_{Top}, and follows the trend of F_{Top} since it contributes by more than 99% towards the F_{Tot}. Any decrease in the flux rate comes from the larger pores occupying more void space and thereby reducing the effective surface area of the catalyst.

Any remaining oxygen at the cathode will diffuse through the pores and down towards the electrolyte interface and eventually to the anode. This may potentially interfere with the glucose oxidation reaction due to the poorer selectivity of the Pt-Ni catalyst. The cathode based on AAO membranes with an original pore size d_{Bot} = 100 nm gives a lower residual DO concentration at

the electrolyte interface inside the fuel cell than the cathodes based on AAO membranes with 200 nm pores, due to larger flux rates of the latter (Figure 5a). This general observation was independent of d_{Top} as well as the catalyst thickness t_m comparing the respective cathodes. However, a larger value of d_{Top} will permit more DO to diffuse past the cathode without being reduced due to a larger radial migration distance from the centre of the pore to the catalyst at the pore rim. In contrast, a thicker catalyst film (t_m) will extend the time available for DO to migrate from the centre to the catalyst that are still present on the wall. Hence, the residual oxygen concentration will increase with d_{Top} but reduces with increasing t_m.

The glucose that diffuses through the pores of the cathode, will continue to diffuse through the electrolyte and be oxidised at the anode. Considering the idealised case where a bulk concentration of 5 mM exists at the surface of the cathode, and zero molar at the anode surface, the concentration of glucose near the pore exit at the electrolyte interface would be equivalent to 2.2 and 3.7 mM for a cathode equipped with d_{Bot} of 100 and 200 nm respectively (Figure 5b).

This concentration difference is limited by the diffusion of glucose through the pore structure over a distance spanning the length of the pores (60 µm). A larger pore permits a higher flux of glucose, whereas an increase in t_m extends the diffusion distance as well as reducing the pore area due to a narrowing of d_{Top}. Hence the glucose concentration at the cathode electrolyte interface decreases slightly with the increase of the catalyst thickness t_m from 100 to 200 nm.

It is clear that the best performance in terms of oxygen reduction will be achieved by reducing the pore size of the cathode in order to maximise its surface area available for catalysis. In contrast, a reduction in the pore size will restrict the flow of glucose to the anode and reduce the catalytic turnover feeding electrons to the oxygen reduction at the cathode. Hence, a balance between the turnover at the cathode and anode is required to find the maximum performance of the complete fuel cell. This should be taken in comparison to the performance achieved in a mixed fuel environment where both glucose and oxygen is free to diffuse to both electrodes.

The simulated relationship between the ideal current density j_{FC} at both electrodes and the geometrics parameters, such as the reduced pore size d_{Top} due to the catalyst deposition, the original pore size d_{Bot} and the catalyst thickness t_m inside the pore, is shown in Figure 6. The simulated values for the ideal current density $|j_{FC}|$ from the cathode shown in Figure 6a are comparable to the theoretically predicted value based on Eq 1 and Eq 4, of 30.1 µA cm^{-2}. This considers a DO concentration gradient of 2 ppm (60 µM). The simulated values shows that the ideal current density decreases with an increase in d_{Bot}, with an increase in the d_{Top} and with a decrease in the catalyst thickness t_m. The higher current densities observed for cathodes equipped with d_{Bot} = 100 nm is due to a larger effective surface area (lower porosity) compared to those equipped with d_{Bot} = 200 nm [25]. Hence, when the surface area reduces with a larger d_{Top} for both electrode types, the performance (and thus the $|j_{FC}|$), is reduced accordingly - a trend that has also been observed by Kerzenmacher [50].

In general, the ideal current density range $|j_{FC}|$ at the cathode obtained in the simulation (27-30 µA cm^{-2}) is higher than the experimentally obtained current density range (< 12 µA cm^{-2}) found from the Pd cathode [25]. The simulation considers a condition in which the reaction kinetics at the surface is faster than the transport by diffusion so that the concentration of reactants at the electrode surface is zero at any time (diffusion limited). Further, it also considers that the reaction products does not obstruct any further supply of reactants. However, the reaction kinetics of the Pd catalyst may be lower than the limiting current as assumed in the model (the concentration of reactants > zero) considered in the model (rate limited).

The ideal current density of the anode (Figure 6b) is greatly influenced by the supply of glucose through the porous cathode and thus mirrors the concentration of glucose seen in figure 5b and with the same factors governing its performance. Thus, a "bulk" concentration ranging from 2.2–3.7 mM inside the fuel cell (Figure 5b), would correspond to a maximum current density ranging from 4.4 – 8.18 μA cm^{-2} (Figure 6b). Experimental data obtained from a similar electrode immersed in 5 mM glucose shows that diffusion limited transport will start to occur above 15 uA cm^{-2} [51]. Although this threshold is expected to scale down with the concentration of glucose (ie 6.6 - 11 uA cm^{-2} respectively) spanning 2.2– 3.7 mM, the modelled power densities should be within the region of rate limitation also in a real device.

A pore density of $1x10^8$ cm^{-2} will give an equivalent porosity of 0.8 to 3.1% considering a pore size of 100 to 200 nm respectively. This is more than one order of magnitude smaller than the average pore density found in a previous study [38] considering a d_{Bot} = 200 nm. Hence it is clear that the DO flux associated with one pore is considerable smaller in a real experimental setting than what the model predicts. Although this can be compensated for by increasing the number of pores in the model (concomitant with a reduction in surface area and F_{Tot} for each pore), the payback will be an increase in the flux of DO and glucose into the fuel cell compartment. However, the pores of the real membrane cannot be treated as a uniform cylinder, but rather as a network of crossing channels, which may increase the diffusion distance and consequently reduce the supply of reagents by diffusion to a similar rate to what the (simplified) model predicts. Thus the modelled pore density represents the best compromise between the two.

3.2 Transport by diffusion II – Balanced current density

We have so far been treating the cathode and anode performance independently from each other. This will not be the case in a stacked fuel cell assembly, where the flow of electrons from the anode would need to balance the reduction reaction at the cathode. Considering electrodes of the same surface area, the cathode cannot have a larger current density than the anode, and there will be a tradeoff where both of these current densities are equal. Since the reaction at the anode is the limiting parameter, the cathode reaction would slow down, creating an abundance of DO at the cathode surface. This DO would diffuse into the fuel cell together with the glucose and potentially become reduced at the anode. This co-oxidation of glucose and reduction of DO will in turn slow down the combined current generation at the anode, which in turn would slow down the reduction rate of DO at the cathode, triggering more DO to diffuse into the pores and down to the anode. Thus, a series of iterative steps were performed using the model to find a balance between the current densities of the electrodes as function of DO and glucose concentration that replicates the ideal conditions using an AAO membrane with pores of 100 and 200 nm and a cathode catalyst film thickness of 200 nm (Figure 6c).

The results show that a cathode with d_{Bot} = 200 nm permits a higher glucose flux rate compared to a cathode with d_{Bot} = 100 nm, which consequently results in a higher current density at the anode which again governs the amount of DO reduced at the cathode surface. An equilibrium condition is expected to be reached around a current density of 4.37 and 7.91 μA cm^{-2} for a stacked fuel cell assembly equipped with cathodes with d_{Bot} of 100 and 200 nm respectively. This corresponds to residual DO at the cathode surfaces of 42 (1.4 ppm) and 35 μM (1.16 ppm) which diffuses into the cell and reacts with the anode, thus reducing the overall current density from that observed in Figure 6b (4.5 and 8.2 μA cm^{-2} respectively).

3.3 Electrochemical Performance

The cell potential and power density for the three experimental cases (section 2.4) are presented in Figure 7. Considering the best case scenario with separated reactants (U1) the fuel cell generated a peak power density of 2.83 ± 0.24 µW cm^{-2} at a current density of 8.2 µA cm^{-2} and an equivalent cell potential of 0.35 ± 0.03 V (Figure 7a). In contrast, the worst case scenario with both reactants supplied to the electrode compartments (U2), a peak power density of 1.61 ± 0.30 µW cm^{-2} was generated at a current density of 6.25 µA cm^{-2} and a cell potential of 0.26 ± 0.04 V (Figure 7b). This reduction in performance (57% of the best case scenario) highlights the need to separate the reagents prior to use. Consequently, the stacked fuel cell assembly simulating the real operating condition (U3) where DO and glucose exists in a mixed fuel environment in which the electrode system was immersed, generated a peak power density of 2.33 ± 0.11 µW cm^{-2} at a current density of 7.7 µA cm^{-2} and a cell potential of 0.30 ± 0.01 V (Figure 7c). The peak power recorded here represented approx. 80% of the value obtained in the best case scenario, suggesting that some separation of the fuels did indeed occur prior to catalysis.

This result (U3) are comparable to the modelled response (d_{Bot} = 200 nm) presented in Figure 6c predicting a peak current density of 7.9 µA cm^{-2}. The differences can be explained from a lower rate of glucose catalysis at the anode and/or a reduced flux of glucose through the embedded Nafion membrane compared to the modelled predictions. There could also have been a larger flux of oxygen reaching the anode and thus reducing the overall net current density from combined glucose oxidation and oxygen reduction reactions. Some glucose could also become oxidised at the cathode, but this has not been considered in the model. The results from the best case scenario (U1) are also comparable to the modelled peak current density of 8.2 µA cm^{-2} supporting the fact that the anode is the current limiting factor in the fuel cell assembly.

A comparison was made with previous work reported in literature using a stacked fuel cell assembly immersed in a mixed fuel environment consisting of comparable values of glucose and oxygen maintained in a physiological phosphate buffer at pH 7.4. It was found that the peak power density of the cell in the mixed fuel environment (U3) was lower than that reported by Kerzenmacher (4.4 ± 0.2 µW cm^{-2}) with a cell using Raney Pt as the catalysts [50]. This is most likely due to a smaller effective surface area of the catalytic layers used in our system due to thinner films compared to that of [50]. Kerzenmacher based his electrodes on a Pt-Al alloy for the cathode (1 µm thick), and a Pt-Zn alloy for the anode (80 µm thick). The power density of our system was also lower than that reported by Rapoport (3.4 µW cm^{-2}). However, his cell was equipped with a Raney Pt-Al anode and a Pt coated cathode of CNT's, running in 10 mM glucose. This was twice the level used in this study. In contrast, the power density was higher than that presented by Oncescu in [44] using comparable film thicknesses and substrate material for the cathode (2 µW cm^{-2}). The reason for this improvement could be the usage of Pd as the oxygen selective catalyst layer at the cathode instead of Pt [44]. The cell was equipped with a cathode made from Pt sputtered on carbon paper. Replacing this cathode with one made from nanoporous AAO resulted in reduced power densities (0.1 – 0.2 µW cm^{-2}). Further, the power density was also higher than the work presented by Stetten (2 µW cm^{-2}), using electrodes made from of activated carbon, and with the anode containing an additional 10% (presumed wt %) of Pt.

The results shows that a fuel cell made from electrodes incorporating thin film evaporated catalysts are able to generate power densities that are comparable to similar reports using electrodes that in part relies on thicker catalyst films. The advantage of thin film technologies is a reduced consumption of (expensive) catalyst and the compatibility with standard silicon

microfabrication. This enables the electrodes to be made by batch fabrication, and also the potential for integration with an associated sensor and electric circuit on the same monolithic chip, enabling the prospect of system integration and further miniaturisation.

The results from the fuel cell experiments were compared to the half-cell measurements obtained in previous studies on the cathodic [25] and the anodic electrode [51] (Figure 8 a,b). Although the results from the cathode (d_{Bot}, t_m = 200 nm) could be compared directly, the electrode potential for the anode had to be calculated based on the curve obtained at 7 ppm DO (sat. air) but adjusted for the offset obtained at 2 ppm [51] and scaled throughout as function of current density. Both electrodes exhibited sensitivities to the fuel/reactant destined for the other electrode as a function of current density, ranging from -22 to -53 mV for the cathode and +100 to +135 mV for the anode - confirming the presence of cross reactions at the electrode surface from both reactants (fuels). By combining the cathodic and anodic curves together one could create a "virtual" cell potential for both the best case (U1) and worst case scenario (U2), and by considering the product with the associated current densities, the equivalent power density curves were calculated (Figure 8 c,d). The different current densities of the cathodic and anodic polarization curves were normalised by extrapolation.

It is clear that the data obtained from the earlier studies does not yield the same performance as that obtained from the direct fuel cell experiments with the best case (U1) in Figure 8 c (1.17 $\mu W\ cm^{-2}$ at 6.6 $\mu A\ cm^{-2}$ and a cell potential of 0.18 volts) being more comparable to the worst case (U2) from Figure 7b (1.61 $\mu W\ cm^{-2}$ at 6.25 6 $\mu A\ cm^{-2}$ and a cell potential of 0.26 volts). One plausible explanation could be the differences in the experimental setup. The studies on the half-cell measurements utilised a common counter electrode (platinum coil) as well as a reference electrode (Ag|AgCl) that could suppress the absolute potentials observed for the cathode as well as the anode. This difference will be strengthened at lower cell potentials supported by the fact that the best case scenario was 1.95 times better than the worst case in the half-cell studies (Figure 8) compared to that found (1.75 times) in the measurements using the electrodes in a fuel cell arrangement (Figure 7).

Another reason is that the electrodes were subject to CV's (from -0.5 to 0.5 V at a scan rate of 0.01 V/s) in air saturated PBS prior to measurements in the fuel cell. This may have removed residual oxides that otherwise would have restricted the catalytic activity, and increasing the open circuit potential (OCP) of the cathode by almost 0.05 volts, suggesting an overall higher cell voltage in the polarization plot.

Long term stability measurements were conducted for 24h in a mixed fuel environment (Figure 9). After an initial decline for the first 4 hours, the potential stabilised for both electrode systems for the duration of the study. Combining these potentials generated an equivalent cell potential in the vicinity of 0.3 V. A more in-depth study of the electrode performances with respect to oxygen and glucose catalysis have previously been reported in [25] for the cathode and [51] for the anode.

4 Conclusions

The separation of glucose and oxygen were successfully demonstrated by experimental observations yielding a power density of the glucose fuel cell package of 2.33 ± 0.11 μW cm^{-2} in a stacked fuel cell assembly. This was 1.45 times higher than that of the cell with separate electrodes working in a mixed fuel environment and approx. 80% of the cell operating with separate reactants. This proof-of-concept study demonstrates that the porous cathode with a Pd catalyst at the top surface do permit the flux of glucose while removing DO that would otherwise migrate to the Raney Pt-Ni catalyst layer at the anode surface. The results were also comparable (albeit better) to prior studies on electrode potentials and polarization using similar electrodes. The differences could be attributed to changes in the electrode arrangement (omitting the counter and reference electrodes) as well as the implementation of a cleaning protocol using CV scans prior to the measurements.

Although a minimal pore diameter (d_{Top} = 100 nm) may be the best way of maximising the surface area of the cathode, it will limit the supply of glucose to the anode. Since the anode is considered being the rate limiting factor, it was found that the larger cathode base diameter (d_{Bot} = 200 nm) yielded the best result. The pore diameter was therefore the governing parameter controlling fuel cell performance with the catalyst thickness t_m acting as a minor correction factor.

Future work will focus on optimising the design by exploring a method in which the porous cathode will be facing down towards the separator membrane. This may reduce the flux rate of DO, but will enhance the conduction of H^+ and thus be a compromise worth exploring as long as the anode represents the limiting factor of the generated current density. Mass-transfer limitations can be enhanced by increasing the porosity of the cathode, by increasing the active area available for substrate diffusion, and by exploring a larger range of the cathodic pore base diameter d_{Bot} to find the maximum pore size before the cathode loose its oxygen scavenging properties. Once confident, the operating ability of the glucose fuel cell should be explored in an endogenous environment inside the body by focusing on the biocompatibility and the effect of the tissue restructuring with time around the fuel cell implant.

Acknowledgements

The authors would like to thank the technical staff and colleagues at University of South-Eastern Norway for their assistance in this work. The work was supported by the Ministry of Church and Education and The Research Council of Norway (Norfab project no. 245963/F50).

References

[1] N. Bhatia, M. El-Chami, Leadless pacemakers: a contemporary review, J Geriatr Cardiol, 15 (2018) 249-253.
[2] S.B. Westerman, M. El-Chami, The subcutaneous implantable cardioverter defibrillator--review of the recent data, J Geriatr Cardiol, 15 (2018) 222-228.
[3] P. Verrills, C. Sinclair, A. Barnard, A review of spinal cord stimulation systems for chronic pain, J Pain Res, 9 (2016) 481-492.
[4] B.H. McAdams, A.A. Rizvi, An Overview of Insulin Pumps and Glucose Sensors for the Generalist, J Clin Med, 5 (2016) 5.
[5] D.A. Gough, L.S. Kumosa, T.L. Routh, J.T. Lin, J.Y. Lucisano, Function of an Implanted Tissue Glucose Sensor for More than 1 Year in Animals, Sci Transl Med, 2 (2010).
[6] F. Moreno, N. Aragon, L. Salazar, In vitro behaviour of interfaces in human molars with an implanted passive RFID microship an subject to compression forces, Dyna-Colombia 80 (2013) 5-10
[7] M.B.B. Martins, F.V.F. de Lima, R.C.J. Santos, A.C.G. Santos, V.M.P. Barreto, E.P.F. de Jesus, Cochlear implants: our experience and literature review, Int Arch Otorhinolaryngol, 16 (2012) 476-481.
[8] A.T. Chuang, C.E. Margo, P.B. Greenberg, Retinal implants: a systematic review, Br J Ophthalmol, 98 (2014) 852.
[9] E. Musk, An Integrated Brain-Machine Interface Platform With Thousands of Channels, J Med Internet Res, 21 (2019) e16194.
[10] V.S. Mallela, V. Ilankumaran, N. Rao, Trends in Cardiac Pacemaker Batteries, Indian Pacing Electrophysiol. J., 4 (2004) 201-212.
[11] B.I. Rapoport, J.T. Kedzierski, R. Sarpeshkar, A Glucose Fuel Cell for Implantable Brain–Machine Interfaces, PLoS One, 7 (2012) e38436.
[12] M.W. Baker, R. Sarpeshkar, Feedback Analysis and Design of RF Power Links for Low-Power Bionic Systems, IEEE Trans Biomed Circuits Syst, 1 (2007) 28-38.
[13] A. Lay-Ekuakille, G. Vendramin, A. Trotta, G. Mazzotta, Thermoelectric generator design based on power from body heat for biomedical autonomous devices, Medical Measurements and Applications, 2009. MeMeA 2009. IEEE International Workshop on, (2009) 1-4.
[14] S.P. Beeby, M.J. Tudor, N.M. White, Energy harvesting vibration sources for microsystems applications, Meas Sci Technol, 17 (2006) R175.
[15] M.E. Nielsen, C.E. Reimers, H.K. White, S. Sharma, P.R. Girguis, Sustainable energy from deep ocean cold seeps, Energy Environ Sci, 1 (2008) 584-593.
[16] I. Ivanov, T. Vidakovic-Koch, K. Sundmacher, Recent Advances in Enzymatic Fuel Cells: Experiments and Modeling, Energies, 3 (2010) 803-846.
[17] T. Yung-Fang, S. Chwen-Jen, Y. Hsiharng, Capillary force pumping fluid for glucose oxidase enzymatic fuel cells, Microsyst. Technol., 23 (2017) 3927–3935.
[18] A.E. Franks, K.P. Nevin, Microbial Fuel Cells, A Current Review, Energies, 3 (2010) 899-919.
[19] R.D. Cusick, B. Bryan, D.S. Parker, M.D. Merrill, M. Mehanna, P.D. Kiely, G. Liu, B.E. Logan, Performance of a pilot-scale continuous flow microbial electrolysis cell fed winery wastewater, Appl Microbiol Biotechnol, 89 (2011) 2053–2063.
[20] M.M. Mardanpour, S. Yaghmaei, Characterization of a microfluidic microbial fuel cell as a

power generator based on a nickel electrode, Biosens Bioelectron, 79 (2016) 327-333
[21] S. Kerzenmacher, J. Ducree, R. Zengerle, F.V. Stetten, Energy harvesting by implantable abiotically catalyzed glucose fuel cells, J. Power Sources, 182 (2008) 1-17.
[22] D. Dector, J.M. Olivares-Ramı´rez, V.M. Ovando-Medina, A. Sosa Dominguez, A.L. Villa, A. Duarte-Moller, N. Sabate´, J.P. Esquivel, A. Dector, Fabrication and evaluation of a passive SU8-based micro direct glucose fuel cell, Microsyst. Technol., 25 (2019) 211–216.
[23] M. Frei, J. Erben, J. Martin, R. Zengerle, S. Kerzenmacher, Nanofiber-deposited porous platinum enables glucose fuel cell anodes with high current density in body fluids, J. Power Sources, 362 (2017) 168-173.
[24] H.-B. Noh, M.H. Naveen, Y.-J. Choi, E.S. Choe, Y.-B. Shim, Implantable nonenzymatic glucose/O-2 micro film fuel cells assembled with hierarchical AuZn electrodes, Chem Commun, 51 (2019) 6659-6662
[25] U.P. Do, F. Seland, M.M. Maharbiz, K. Wang, Ø. Johannesen, E.A. Johannessen, Thin film nanoporous electrodes for the selective catalysis of oxygen in abiotically catalysed micro glucose fuel cells, J. Mater. Sci., 51 (2016) 9095-9107.
[26] V.S. Bagotzky, Y.B. Vasilyev, Some characteristics of oxidation reactions of organic compounds on platinum electrodes, Electrochim Acta, 9 (1964) 869-882.
[27] R.A. Escalona-Villalpando, K. Hasan, R.D. Milton, A. Moreno-Zuria, L.G. Arriaga, S.D. Minteer, J. Ledesma-García, Performance comparison of different configurations of Glucose/O2 microfluidic biofuel cell stack, J. Power Sources, 414 (2019) 150-157.
[28] F. Pan, T. Samaddar, Charge Pump Circuit Design, McGraw-Hill Professional, New York, 2006.
[29] C. Agnes, M. Holzinger, A. Le Goff, B. Reuillard, K. Elouarzaki, S. Tingry, S. Cosnier, Supercapacitor/biofuel cell hybrids based on wired enzymes on carbon nanotube matrices: autonomous reloading after high power pulses in neutral buffered glucose solutions, Energy Environ Sci, 7 (2014) 1884-1888.
[30] Y. Li, D. Zhao, W.A. Serdijn, A Sub-Microwatt Asynchronous Level-Crossing ADC for Biomedical Applications, IEEE Trans Biomed Circuits Syst, 7 (2013) 149-157.
[31] A. Kempitiya, D.-A. Borca-Tasciuc, M.M. Hella, Low-Power ASIC for Microwatt Electrostatic Energy Harvesters, IEEE Trans. Ind. Electron., 60 (2013) 5639-5647.
[32] M. Merenda, D. Iero, F.G. Della Corte, CMOS RF Transmitters with On-Chip Antenna for Passive RFID and IoT Nodes, Electronics, 8 (2019) 1448.
[33] S. Kerzenmacher, M. Schroeder, R. Bramer, R. Zengerle, F. von Stetten, Raney-platinum film electrodes for potentially implantable glucose fuel cells. Part 1: Nickel-free glucose oxidation anodes, J. Power Sources, 195 (2010) 6516-6523.
[34] A. Kloke, B. Biller, S. Kerzenmacher, U. Kräling, R. Zengerle, F.v. Stetten, A single layer biofuel cell as potential coating for implantable low power devices, Proceeding of Eurosensors, (2008) 1416-1419.
[35] A. Kozawa, V.E. Zilionis, R.J. Brodd, Electrode Materials and Catalysts for Oxygen Reduction in Isotonic Saline Solution, J Electrochem Soc, 117 (1970) 1474-1478.
[36] W. Sun, A. Hsu, R. Chen, Palladium-coated manganese dioxide catalysts for oxygen reduction reaction in alkaline media, J. Power Sources, 196 (2011) 4491-4498.
[37] O. Savadogo, K. Lee, K. Oishi, S. Mitsushima, N. Kamiya, K.I. Ota, New palladium alloys catalyst for the oxygen reduction reaction in an acid medium, Electrochem commun, 6 (2004)

105-109.
[38] U.P. Do, F. Seland, E.A. Johannessen, The Real Area of Nanoporous Catalytic Surfaces of Gold and Palladium in Aqueous Solutions, J Electrochem Soc, 165 (2018) H219-H228.
[39] A. Brouzgou, P. Tsiakaras, Electrocatalysts for Glucose Electrooxidation Reaction: A Review, Top Catal, 58 (2015) 1311-1327.
[40] R.R. Adzic, M.W. Hsiao, E.B. Yeager, Electrochemical oxidation of glucose on single crystal gold surfaces, J. electroanal. chem. interfacial electrochem., 260 (1989) 475-485.
[41] A. Brouzgou, A. Podias, P. Tsiakaras, PEMFCs and AEMFCs directly fed with ethanol: a current status comparative review, J Appl Electrochem, 43 (2013) 119-136.
[42] R. Parsons, T. VanderNoot, The oxidation of small organic molecules, J. electroanal. chem. interfacial electrochem., 257 (1988) 9-45.
[43] U. Gebhardt, J.R. Rao, G.J. Richter, A special type of raney-alloy catalyst used in compact biofuel cells, J Appl Electrochem, 6 (1976) 127-134.
[44] V. Oncescu, D. Erickson, A microfabricated low cost enzyme-free glucose fuel cell for powering low-power implantable devices, J. Power Sources, 196 (2011) 9169-9175.
[45] R.F. Drake, B.K. Kusserow, S. Messinger, S. Matsuda, A tissue implantable fuel cell power supply, Trans. Ams. Soc. Artif. Intern. Organs, 16 (1970) 199-205.
[46] J.R. Rao, G. Richter, E. Weidlich, F. von Sturm, Metal-Oxygen and Glucose-Oxygen Cells As Power Sources for Implantable Devices, Phys. Med. Biol., 17 (1972).
[47] F. von Sturm, G. Richter, in: U.P. Office (Ed.), Siemens Aktiengesellschaft, USA, 1976.
[48] F. von Stetten, S. Kerzenmacher, R. Sumbharaju, R. Zengerle, J. Ducrée, Biofuel cells as micro power generators for implantable devices, Proceedings of Eurosensors (2006) 222-225.
[49] B.-Y. Song, Y. He, Y.-L. He, D. Huang, Y.-W. Zhang, Experimental study on anode components optimization for direct glucose fuel cells, Energy, 176 (2019) 15-22.
[50] S. Kerzenmacher, U. Kraling, T. Metz, R. Zengerle, F. von Stetten, A potentially implantable glucose fuel cell with Raney-platinum film electrodes for improved hydrolytic and oxidative stability, J. Power Sources, 196 (2011) 1264-1272.
[51] U.P. Do, F. Seland, K. Wang, E.A. Johannessen, Raney-platinum thin film electrodes for the catalysis of glucose in abiotically catalyzed micro-glucose fuel cells, J. Mater. Sci., (2019).
[52] J. Peron, A. Mani, X. Zhao, D. Edwards, M. Adachi, T. Soboleva, Z. Shi, Z. Xie, T. Navessin, S. Holdcroft, Properties of Nafion® NR-211 membranes for PEMFCs, J Memb Sci, 356 (2010) 44-51.
[53] D.P.M. Northmore, J.G. Elias, in: Proc. first IEEE World Congress on Computational Intelligence, Orlando, FL, 1994, pp. 753-758.
[54] S. Li, Chapter 13 - Introduction to Electrochemical Reaction Engineering, in: S. Li (Ed.) Reaction Engineering, Butterworth-Heinemann (Elsevier), 2017, pp. 599-651.
[55] S. Kerzenmacher, J. Ducree, R. Zengerle, F.v. Stetten, An abiotically catalyzed glucose fuel cell for powering medical implants: Reconstructed manufacturing protocol and analysis of performance, J. Power Sources, 182 (2008) 66-75.
[56] E.M. Renkin, Filtration, diffusion, and molecular sieving through porous cellulose membranes, J Gen Physiol, 38 (1954) 225-243.
[57] R.E. Beck, J.S. Schultz, Hindrance of solute diffusion within membranes as measured with microporous membranes of known pore geometry, Biochim Biophys Acta, 255 (1972) 273-303.
[58] T.K. Goldstick, V.T. Ciuryla, L. Zuckerman, Diffusion of oxygen in plasma and blood, Adv Exp Med Biol, 75 (1970) 183-190.

[59] E.L. Cussler, Diffusion: Mass Transfer in Fluid Systems, 3 ed., Cambridge University Press, Cambridge, 2009.

Figure legends

Figure 1: Schematic representation of the fuel cell assembly

Figure 2: (a) The model with the geometrical parameters used in the simulation. (b) The diffusion coefficient of glucose and DO inside the pore vs the pore diameter.

Figure 3: Two experiment set up (a) U-tube cell (b) stacked fuel cell assembly, and (c) cross section.

Figure 4: The DO flux associated with a single pore element at the cathode surface as a function of the original pore size (d_{Bot}) and the catalyst thickness (t_m). (a) The oxygen flux at the inclined section of the pore wall (F_{Incl}), and (b) the total flux (F_{Tot}) considering the combined DO reduction at the top surface and the inclined pore wall.

Figure 5: The concentration of (a) DO and (b) glucose at the cathode-electrolyte interface (inside the fuel cell) as a function of pore size (d_{Top}) and catalyst thickness (t_m). Inset (i) and (ii) depicts the narrow concentration changes for glucose diffusing through a cathode with d_{Bot} of 200 and 100 nm respectively. The simulation consider concentration gradients in an idealized case where all DO is completely reduced at the cathode surface (incl. the pore rim) and all the glucose is completely oxidized at the anode.

Figure 6: The current density of (a) the cathode and (b) the anode as a function of pore size (d_{Top}) and catalyst thickness (t_m) of the cathode. Inset (i) and (ii) depicts the narrow changes in current density at the anode as a function of the cathode type used (d_{Bot} of 200 and 100 nm respectively) through which glucose is diffusing. The simulation consider concentration gradients in an idealized case where all DO is completely reduced at the cathode surface (incl. the pore rim) and all the glucose is completely oxidized at the anode. (c) Current densities as function of pore radius (d_{Top}), oxygen concentrations (C_{DO}) at the cathode surface and effective “bulk” concentrations of glucose (C_{glu}) inside the fuel cell. The film thickness of the cathode catalyst was t_m= 200 nm.

Figure 7: Polarizarion curves obtained from the fuel cell representing (a) the best case scenario (U1) with separate fuels at the anode and cathode; (b) the worst case scenario (U2) in which both reagents are mixed, and (c) using a stacked fuel cell assembly (U3) attempting a separation of the fuels in a mixed fuel environment. The error bars correspond to ± 1 std dev, n = 3 number of measurements.

Figure 8: (a) Cathodic polarisation curves at constant 2 ppm DO in the absence and presence of glucose, and (b) anodic polarisation curves at constant 5 mM glucose in the absence and presence of DO. The corresponding cell potentials and power densities were calculated from the two electrode potentials considering (c) separate fuels - best case, and (d) mixed fuels - worst case. The data was extracted and rearranged from [25],[51] for comparison.

Figure 9: Long term stability measurements combining anodic and cathodic potentials in a mixed fuel environment at a constant current density of 2 μA cm^{-2}. The data was extracted and rearranged from [25],[51] for comparison.

Figures

Figure 1

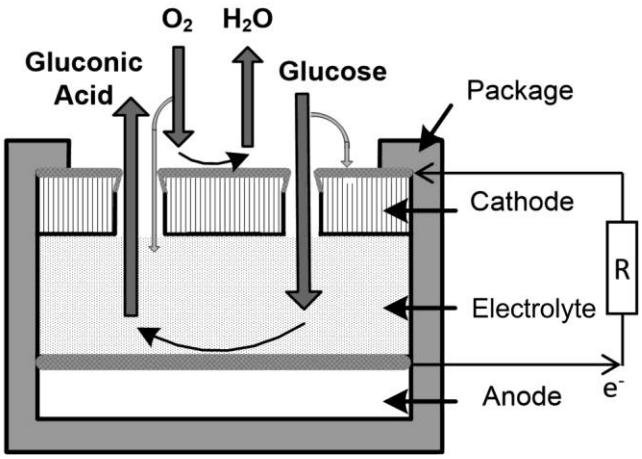

Figure 2

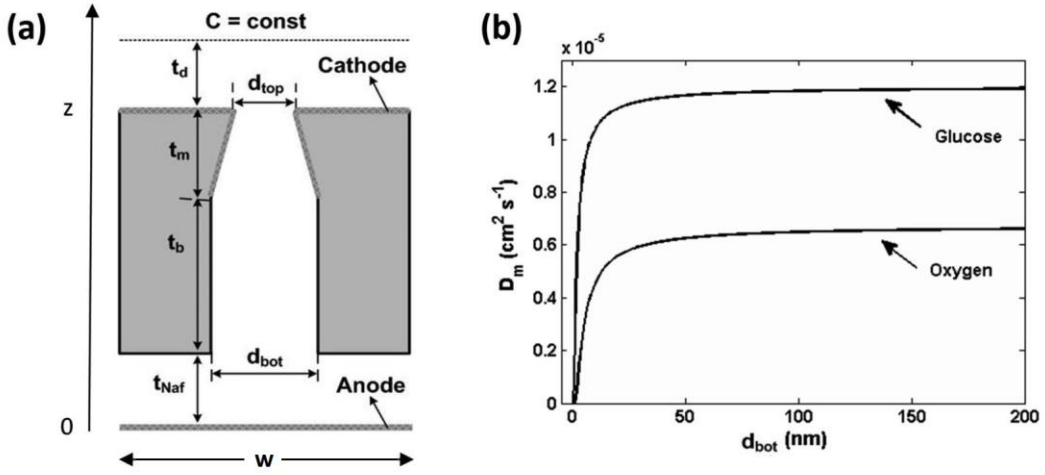
(a)
C = const
Cathode
t_d
d_{top}
z
t_m
t_b
d_{bot}
t_{Naf}
Anode
0
w
(b)
x 10^{-5}
1.2
1
0.8
0.6
0.4
0.2
0
D_m (cm^2 s^{-1})
Glucose
Oxygen
0
50
100
150
200
d_{bot} (nm)

Figure 3

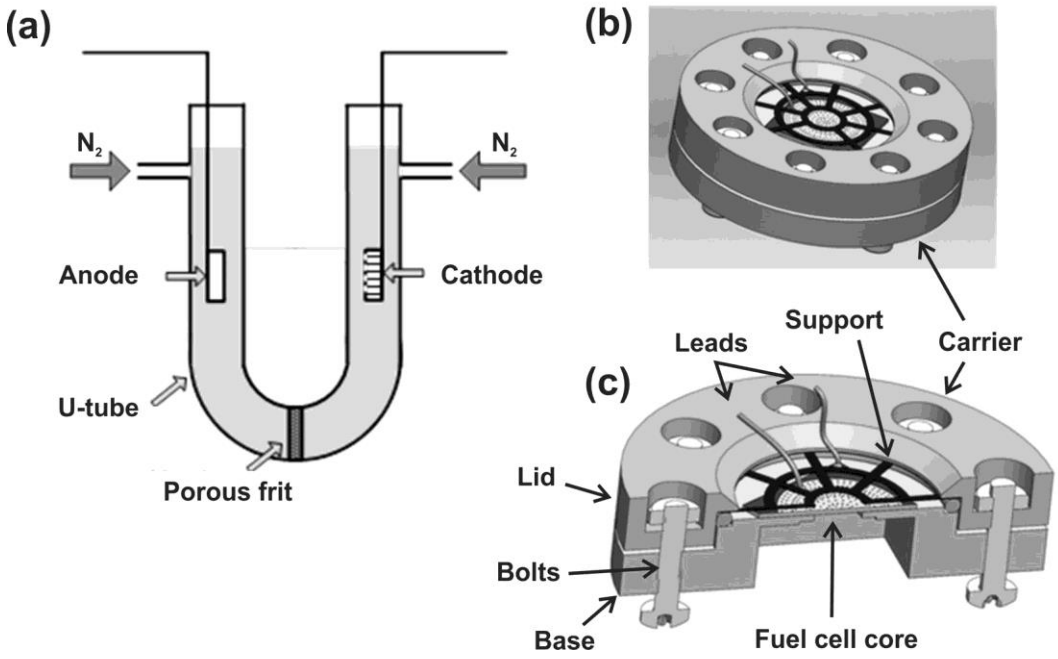
(a)
N2
N2
Anode
Cathode
U-tube
Porous frit
(b)
Carrier
(c)
Leads
Support
Lid
Bolts
Base
Fuel cell core

Figure 4

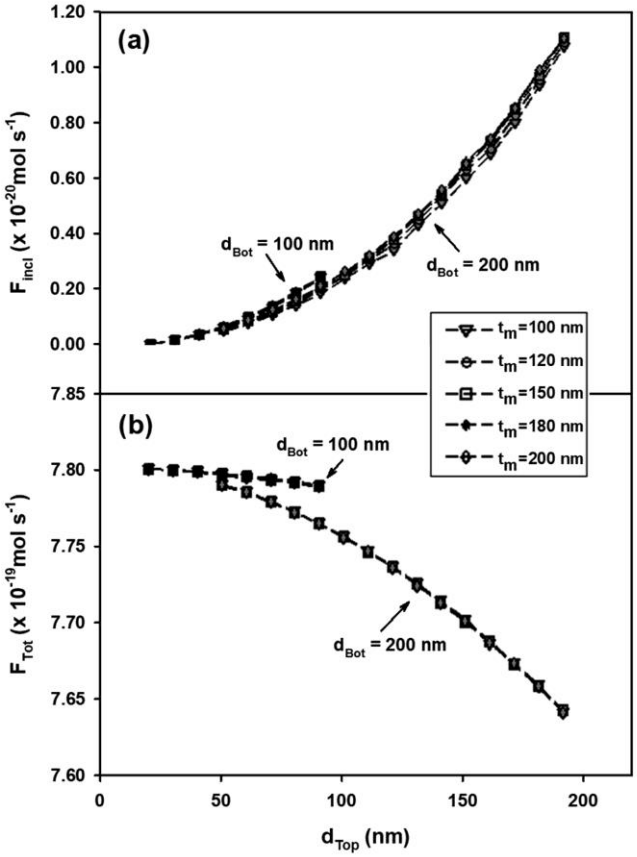
(a)
(b)
F_{incl} (x 10^{-20}mol s^{-1})
F_{Tot} (x 10^{-19}mol s^{-1})
d_{Top} (nm)
d_{Bot} = 100 nm
d_{Bot} = 200 nm
t_m=100 nm
t_m=120 nm
t_m=150 nm
t_m=180 nm
t_m=200 nm
1.20
1.00
0.80
0.60
0.40
0.20
0.00
7.85
7.80
7.75
7.70
7.65
7.60
0
50
100
150
200

Figure 5

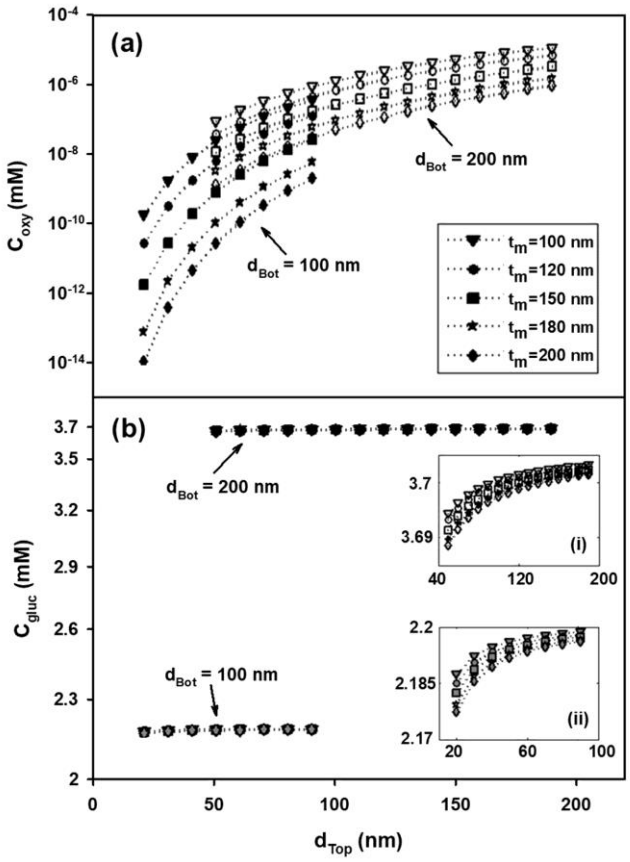
(a)
C_{oxy} (mM)
10^{-4}
10^{-6}
10^{-8}
10^{-10}
10^{-12}
10^{-14}
d_{Bot} = 200 nm
d_{Bot} = 100 nm
t_m=100 nm
t_m=120 nm
t_m=150 nm
t_m=180 nm
t_m=200 nm
(b)
C_{gluc} (mM)
3.7
3.5
3.2
2.9
2.6
2.3
2
d_{Bot} = 200 nm
d_{Bot} = 100 nm
3.7
3.69
(i)
40
120
200
2.2
2.185
2.17
(ii)
20
60
100
0
50
100
150
200
d_{Top} (nm)

Figure 6

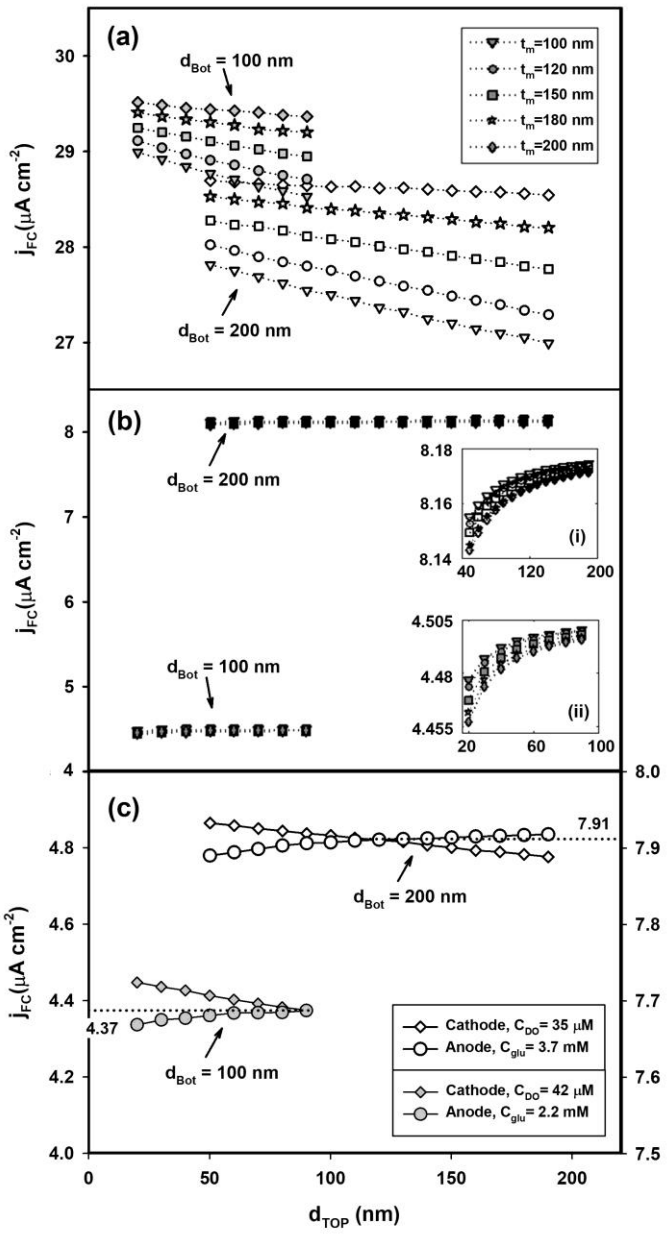
(a)
d_{Bot} = 100 nm
d_{Bot} = 200 nm
t_m=100 nm
t_m=120 nm
t_m=150 nm
t_m=180 nm
t_m=200 nm
(b)
d_{Bot} = 200 nm
d_{Bot} = 100 nm
(i)
(ii)
(c)
7.91
d_{Bot} = 200 nm
4.37
d_{Bot} = 100 nm
Cathode, C_{DO}= 35 μM
Anode, C_{glu}= 3.7 mM
Cathode, C_{DO}= 42 μM
Anode, C_{glu}= 2.2 mM
j_{FC}(μA cm^{-2})
d_{TOP} (nm)

Figure 7

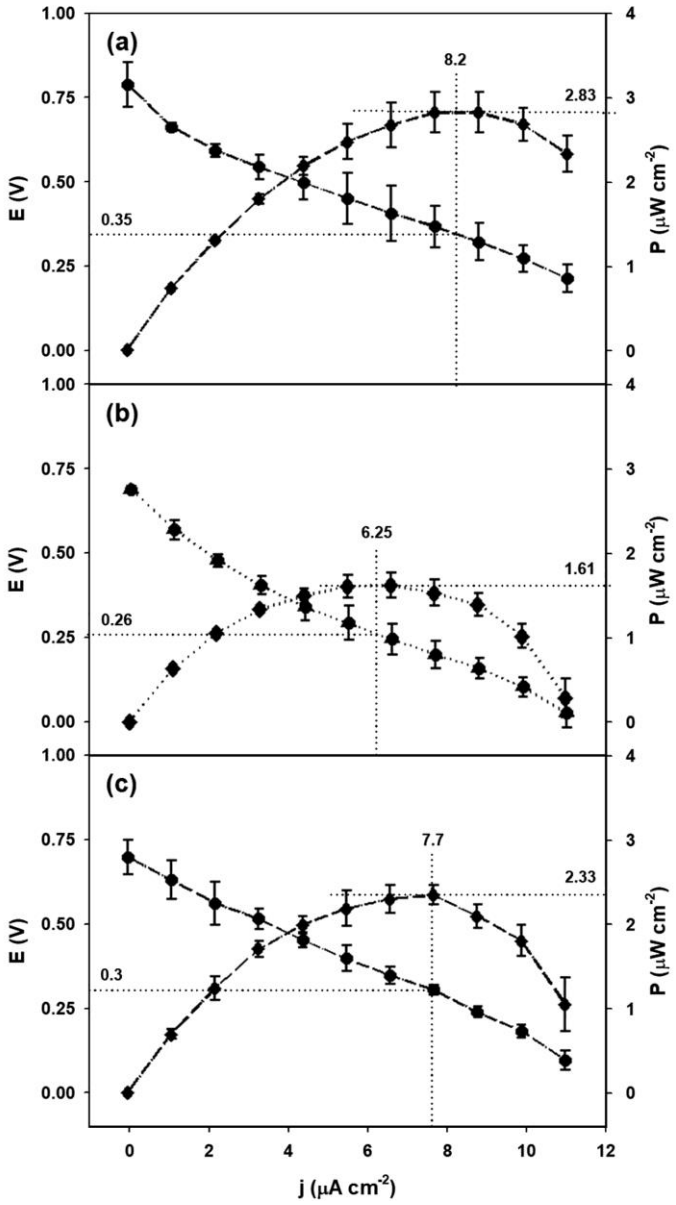

Figure 8

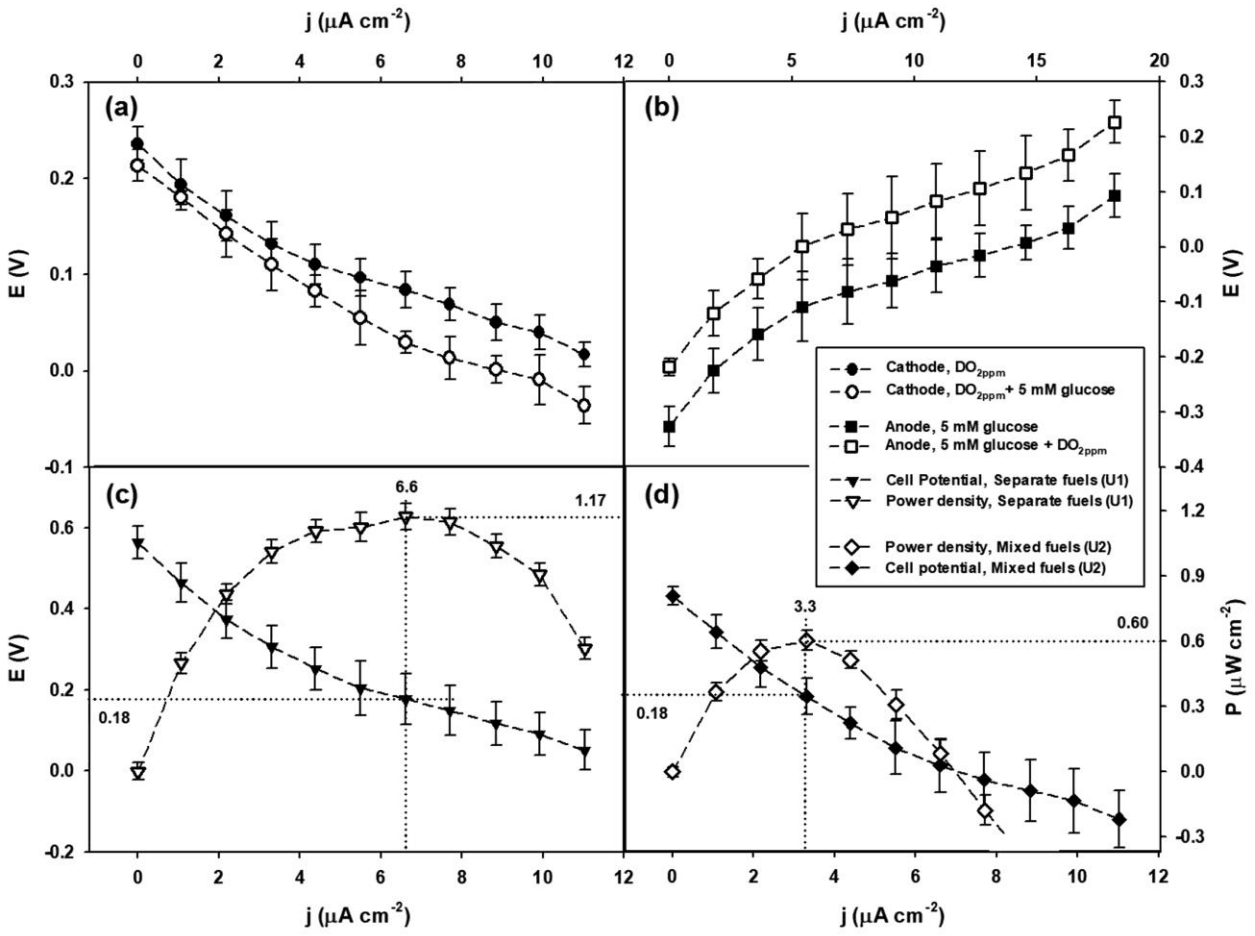
(a)
(b)
(c)
(d)
j (μA cm-2)
E (V)
P (μW cm-2)
Cathode, DO2ppm
Cathode, DO2ppm + 5 mM glucose
Anode, 5 mM glucose
Anode, 5 mM glucose + DO2ppm
Cell Potential, Separate fuels (U1)
Power density, Separate fuels (U1)
Power density, Mixed fuels (U2)
Cell potential, Mixed fuels (U2)
6.6
1.17
0.18
3.3
0.60
0.18

Figure 9